Application of Unfitted Finite Element Methods for Estimating Added Mass and Added Damping in Floating Structures

Modderman, Jan; Colomés, Oriol

DOI
10.3934/acse.2025015

Publication date
2025

Document Version
Final published version

Published in
Advances in Computational Science and Engineering

Advances in Computational Science and Engineering
Vol. 4, 2025, pp. 142-167
doi:10.3934/acse.2025015

APPLICATION OF UNFITTED FINITE ELEMENT METHODS FOR ESTIMATING ADDED MASS AND ADDED DAMPING IN FLOATING STRUCTURES

Jan Modderman[✉*1] and Oriol Colomés[✉1]

[1]Delft University of Technology, The Netherlands

Abstract. The development of accurate and efficient methods for hydrodynamic analysis of floating structures is essential for advancing offshore renewable energy technologies. In this work, we evaluate three unfitted Finite Element methods: the Shifted Boundary Method, the Cut Finite Element Method, and the Aggregated Unfitted Finite Element Method. These three methods are assessed for the estimation of added mass and damping coefficients of floating structures in two dimensions. These methods eliminate the need for traditional meshing, simplifying the analysis of complex geometries, particularly those with sharp edges, in the frequency domain using linear potential flow theory. We present a novel implementation of these techniques, highlighting their ability to handle multiple geometries with a single background mesh while maintaining high accuracy. Results are validated against experimental, numerical, and analytical benchmarks, demonstrating good agreement. This work not only highlights the potential of unfitted Finite Element methods for efficient and accurate hydrodynamic analysis but also identifies key challenges and knowledge gaps to guide future advancements in wave-structure interaction modeling.

1. **Introduction.** The need for fast, accurate, and automated assessment is becoming critical to ensure the safety, performance, and economic feasibility of many engineering problems. This is particularly the case for offshore renewable energy technologies, such as offshore wind and wave energy converters, which play a crucial role in the transition towards renewable energies. In such a context, floating structures are key components to ensure the feasibility of this transition. As the demand for efficient and sustainable offshore energy solutions grows, the design and analysis of floating structures must evolve to meet the challenges of complex environmental conditions and large-scale deployments. Efficient and streamlined design processes are necessary for delivering optimal solutions within tight timeframes.

In the preliminary design phase of floating structures in offshore environments, it is common to use potential flow theory for the hydrodynamic analysis, assuming incompressible and irrotational flow, and neglecting viscous effects. Moreover, the hydrodynamic assessment of offshore structures can be further simplified by assuming waves with small steepness, leading to the linearized potential flow theory, or

2020 *Mathematics Subject Classification.* Primary: 76Bxx, 65Nxx.

Key words and phrases. Unfitted Finite Element methods, linear potential flow, Shifted Boundary Method, aggregated finite element method, cut Finite Element method, frequency domain analysis, floating structures.

*Corresponding author: Jan Modderman.

Airy theory for waves in deep waters [2]. Under these idealized conditions, and further assuming simplified geometries, such as structures with regular geometries and bathymetry, analytical or semi-analytical methods can be effectively used to estimate hydrodynamic loads and structural responses of floating structures, see e.g. [22]. However, as floating structures become more complex in shape or operate in more challenging wave conditions and bathymetries, these simplifications are no longer applicable.

In these cases, numerical methods are required to account for arbitrary geometries, nonlinearities, and more realistic environmental conditions. The Boundary Element Method (BEM) is a widely used numerical method in offshore engineering to solve wave-structure interaction problems [28]. In BEM, the discrete problem is reduced to the boundary, reducing the amount of discrete unknowns of the system. However, its applicability is limited by the high computational demands for large-scale simulations, due to the dense algebraic systems that arise [35]. These challenges become even more pronounced when dealing with nonlinear potential flow theory, and particularly for large-scale or multiple structures. In contrast, volume discretization methods such as the Finite Difference (FD) or the Finite Element Method (FEM) become more competitive, especially for complex geometries and/or nonlinear problems, as they are more flexible and can accommodate scalable solvers for large-scale simulations. In this work, we will focus on the use of a FEM approach for the solution of potential flow theory in the context of floating structures, as pioneered in [37, 38]. Other approaches based on the FD method or Spectral Methods can also lead to more efficient solutions than BEM for large problems, see for instance [10, 17, 40]. A prominent feature of FEM for the solution of wave-structure interaction problems is that it naturally allows for a monolithic coupling between fluid and elastic structures, which is particularly relevant when modeling large and flexible floating platforms [14, 1].

Novel solutions for floating structures often require designs with complex geometrical shapes, which make the meshing process required for numerical methods both challenging and time-consuming. When dealing with complex and/or non-watertight geometry representations, such as Standard Tessellation Language (STL) files, generating a suitable mesh may become impractical or even impossible. This bottleneck highlights the relevance of unfitted (also known as immersed or embedded) discretization methods, which significantly streamline and simplify the meshing process, offering greater flexibility and efficiency. In the context of wave-structure interaction assessment, many works are recently gaining attention in related topics, specially due to the benefits they can bring to accurately calculate 2nd order effects in geometries with sharp features. This is the case of the work presented in [36], where the authors present an XFEM approach for hydrodynamic analysis of 2D structures. Similarly, in [41, 30] the authors propose a high-order immersed boundary method using a FD and Harmonic Polynomial Cell approaches, respectively, that overcomes the spurious oscillations in time that typically arise in such approaches for moving domains, see e.g. [24, 21].

In a FEM context, unfitted approaches may also lead to spurious force oscillations in time due to inaccurate mass conservation in problems with moving domains. In [13] the authors propose a weighted Shifted Boundary Method (WSBM) for free surface flows that reduces the spurious force oscillations due to mass conservation errors, preserving the optimal accuracy of the underlying finite element space. This approach has also been recently extended to fluid-structure interaction problems in

[39]. The WSBM is based on the original Shifted Boundary Method (SBM), which has been demonstrated to be an efficient unfitted FEM approach for several problems, see for example [26, 29, 3, 4]. The SBM has also been recently used in the context of wave-structure interaction problems [32] or to solve high-order potential flow problems with spectral elements [33]. In the last decade, other unfitted FEM approaches have been proposed to deal with problems with complex geometries. The Cut Finite Element Method (CutFEM) is one of the most popular techniques [12], which has also been used for the solution of potential flow problems, e.g. [15]. In the CutFEM and WSBM approaches, ghost penalty stabilization [11] is required to prevent ill-conditioning of the resulting system. Alternatively, in [8] the authors introduced the Aggregated unfitted Finite Element Method (AgFEM), where they propose a cell-aggregation technique that overcomes the need for additional stabilization terms. The AgFEM method has also been extended to the cases of nonlinear geometry [27] and high-order finite elements [6].

In this work, we evaluate the previously described unfitted FEM techniques, i.e. SBM, CutFEM, and AgFEM, for characterizing hydrodynamic coefficients of floating structures. By eliminating the need for a meshing step, these methods simplify the modeling of wave-structure interactions for complex geometries in 2D, with special focus in the case of geometries with sharp edges. For the sake of simplicity and without losing the generality of the methods analyzed, this study focuses on the frequency-dependent characterization of added mass and damping coefficients. To validate and demonstrate the methods, we present benchmark test cases, highlighting the effectiveness of these approaches in complex scenarios. This work demonstrates the novel application of AgFEM, CutFEM, and SBM to the estimation of added mass and added damping in 2D. The cases are verified using the work of Wang et al.[36]. For SBM, the surface shifting using Jacobian operators is addressed.

In Section 2, the physical problem is introduced and the approach is derived to estimate the added mass and the added damping. In Section 3, the unfitted FE methods aforementioned are introduced, commonalities between the methods are highlighted, and modifications for the estimation of hydrodynamic coefficients are presented. In Section 4, several case studies are presented, namely, a heaving rectangle, which is compared to other numerical approaches and experimental data, and a horizontal cylinder at varying depths of submergence that is compared to analytical data. Additionally, we consider a sensitivity analysis on the ghost penalty parameter, and we compare the condition number between the unfitted methods. In Section 5, some conclusions are presented and future research is suggested.

2. **Problem setting.**

In Figure 1 we depict the domain of a simple surface-piercing structure floating in a free-surface flow problem. For simplicity, we assume that the seabed is flat and horizontal. Thus, the domain consists of a topological cube, here depicted in 2 dimensions. The free surface Γ_f is at the top of the domain. We assume that the floating object can be characterised by some length parameter D and its interface with the fluid is denoted by Γ. At the bottom there is the seabed boundary Γ_{sb} and at the left and right boundaries there are the inlet Γ_{in} and the outlet Γ_{out}. The interior domain, assumed to be water, is the domain enclosed by these boundaries, Ω.

2.1. **Governing equations.**

The governing equations for fluid-structure interaction are typically the Navier-Stokes equations for fluid dynamics and linear elasticity

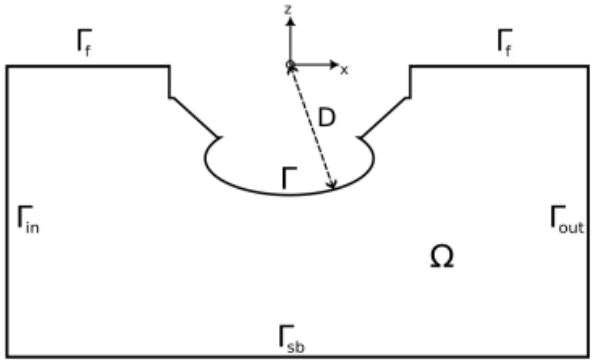

FIGURE 1. Overview of a general domain with boundaries and length characteristics.

equations for structural mechanics. In offshore engineering applications, the structure is typically simplified to be a rigid object, hence applying Newton's second law for the definition of the equation of motion. For the governing equations of the fluid, the fluid is assumed to be incompressible, inviscid, and irrotational, such that potential flow theory can be applied.

From the continuity equation, assuming incompressible flow and introducing the Bernoulli equation at the free surface boundary, the resulting strong form of the fluid problem with corresponding boundary conditions reads:

$$\Delta\phi = 0 \quad \text{in} \quad \Omega, \tag{1a}$$

$$\frac{\partial\eta}{\partial t} + \tilde{\nabla}\phi \cdot \tilde{\nabla}\eta - \nabla\phi \cdot \boldsymbol{n}_z = 0 \quad \text{on} \quad \Gamma_f, \tag{1b}$$

$$\frac{\partial\phi}{\partial t} + \frac{1}{2}|\nabla\phi|^2 + g\eta = 0 \quad \text{on} \quad \Gamma_f, \tag{1c}$$

$$\nabla\phi \cdot \boldsymbol{n}_z = 0 \quad \text{on} \quad \Gamma_{sb}, \tag{1d}$$

$$\nabla\phi \cdot \boldsymbol{n}_{in} = v_{in} \quad \text{on} \quad \Gamma_{in}, \tag{1e}$$

$$\nabla\phi \cdot \boldsymbol{n}_{out} = v_{out} \quad \text{on} \quad \Gamma_{out}. \tag{1f}$$

Here, ϕ is the velocity potential, η is the scalar free surface elevation, the operator $\tilde{\nabla} = (\frac{\partial}{\partial x}, \frac{\partial}{\partial y})$ is the gradient operator in the horizontal plane, $\boldsymbol{n}$ denotes the normal vector to the respective surfaces or in the vertical z-direction and g is the gravitational constant. We assign an input velocity v_{in} and an output velocity v_{out}, which are defined in Section 4.

The structure is treated as a rigid body. In this work, we assume that the motion is limited to translational motion. For a more general scenario, a six degrees of freedom system (in 3D) could be applied. In such a case, the methods described do not differ, and for the sake of simplicity, we focus only on the translations, i.e. surge, sway and heave motions in naval naming convention, which is governed by:

$$\boldsymbol{M}\frac{\partial^2\mathbf{u}}{\partial t^2} = \boldsymbol{f}_{\text{ext}}, \tag{2}$$

where $\boldsymbol{M}$ is the mass matrix of the structure, $\mathbf{u}$ the displacement vector, and $\boldsymbol{f}_{\text{ext}}$ resulting external forces. These forces arise from pressure on the wet surface. That is,

$$\boldsymbol{f}_{\text{ext}} = -\int_{\Gamma} p\boldsymbol{n}_{\Gamma}\, d\Gamma, \quad \text{with} \quad p = \rho\frac{\partial\phi}{\partial t} + \frac{1}{2}|\nabla\phi|^2 + \rho g\mathbf{u}\cdot\boldsymbol{n}_z. \tag{3}$$

Generally, considering potential flow for offshore engineering applications, it is common to only consider first order effects [25]. Linearization is accomplished by neglecting the non-linear terms. The so-called reduced formulation is then introduced by substituting the first time derivative of equation (1c) into equation (1b). Thereby eliminating the scalar free surface elevation η from the problem description. For consistency, we will also neglect the nonlinear terms in the governing equation for the structure. Thus, the coupled system accounting for fluid, equation (1), and rigid body dynamics, equation (2), leads to the following linearized strong form:

$$\Delta\phi = 0 \quad \text{in} \quad \Omega, \tag{4a}$$

$$\frac{\partial^2\phi}{\partial t^2} + g\nabla\phi\cdot\boldsymbol{n}_z = 0 \quad \text{on} \quad \Gamma_f, \tag{4b}$$

$$\nabla\phi\cdot\boldsymbol{n}_z = 0 \quad \text{on} \quad \Gamma_{sb}, \tag{4c}$$

$$\nabla\phi\cdot\boldsymbol{n}_{in} = v_{in} \quad \text{on} \quad \Gamma_{in}, \tag{4d}$$

$$\nabla\phi\cdot\boldsymbol{n}_{out} = v_{out} \quad \text{on} \quad \Gamma_{out}, \tag{4e}$$

$$(\nabla\phi - \frac{\partial\mathbf{u}}{\partial t})\cdot\boldsymbol{n}_{\Gamma} = 0 \quad \text{on} \quad \Gamma, \tag{4f}$$

$$\boldsymbol{M}\frac{\partial^2\mathbf{u}}{\partial t^2} + \int_{\Gamma}\left[\left(\rho\frac{\partial\phi}{\partial t} + \rho g\mathbf{u}\cdot\boldsymbol{n}_z\right)\boldsymbol{n}_{\Gamma}\right] d\Gamma = \mathbf{0} \quad \text{on} \quad \Gamma. \tag{4g}$$

2.1.1. *Linear potential flow in frequency domain.* The resulting system of equations (4) is linear and, therefore, it is convenient to analyze it in the frequency domain. That is, we assume the potential field and vertical displacement can be decomposed in a Fourier series,

$$\phi(\mathbf{x}, t) = \sum_{k=1}^{\infty}\hat{\phi}_k(\mathbf{x})\exp\left(-i\omega_k t + \psi_k\right), \tag{5}$$

$$\mathbf{u}(t) = \sum_{k=1}^{\infty}\hat{\mathbf{u}}_k\exp\left(-i\omega_k t + \psi_k\right). \tag{6}$$

Where $\hat{\phi}_k$ and $\hat{\mathbf{u}}_k$ are complex-valued time-independent amplitudes associated with each frequency ω_k and phase shift ψ_k. Applying the superposition principle of linear systems, we can solve independent linear problems for each frequency in the Fourier decomposition (5). Thus, for a given term of the Fourier expansion with associated frequency ω_k, the resulting problem reads

$$\Delta\hat{\phi}_k = 0 \quad \text{in} \quad \Omega, \tag{7a}$$

$$-\omega_k^2\hat{\phi}_k + g\nabla\hat{\phi}_k\cdot\boldsymbol{n}_z = 0 \quad \text{on} \quad \Gamma_f, \tag{7b}$$

$$\nabla\hat{\phi}_k\cdot\boldsymbol{n}_z = 0 \quad \text{on} \quad \Gamma_{sb}, \tag{7c}$$

$$\nabla\hat{\phi}_k\cdot\boldsymbol{n}_{in} = v_{in}^k \quad \text{on} \quad \Gamma_{in}, \tag{7d}$$

$$\nabla\hat{\phi}_k\cdot\boldsymbol{n}_{out} = v_{out}^k \quad \text{on} \quad \Gamma_{out}, \tag{7e}$$

$$\nabla\phi\cdot\boldsymbol{n}_{\Gamma} + i\omega_k\hat{\mathbf{u}}_k\cdot\boldsymbol{n}_{\Gamma} = 0 \quad \text{on} \quad \Gamma, \tag{7f}$$

$$-\omega_k^2 \boldsymbol{M}\hat{\mathbf{u}}_k + \int_\Gamma \left[\left(-i\omega\rho\hat{\phi}_k + \rho g \hat{\mathbf{u}}_k \cdot \boldsymbol{n}_z\right)\boldsymbol{n}_\Gamma\right] d\Gamma = \mathbf{0} \qquad \text{on} \quad \Gamma. \tag{7g}$$

In what follows we will describe the formulation for the linear potential flow problem in frequency domain defined in equation (7). To simplify notation hereinafter, we drop the hat sign and the sub-index k, that is: $\phi \doteq \hat{\phi}_k$, $\mathbf{u} \doteq \hat{\mathbf{u}}_k$ and $\omega \doteq \omega_k$.

2.2. **The discrete problem.** Before deriving the discrete problem of the coupled system (7), we introduce some notation that will be used hereafter. The spaces of functions whose p-th power is absolutely integrable in Ω are denoted by $L^p(\Omega)$, $1 \leq p < \infty$. For $p = 2$, this becomes a Hilbert space with the scalar product

$$(u, v)_\Omega \doteq (u, v) := \int_\Omega u(\mathbf{x})\, v(\mathbf{x})\, d\Omega \tag{8}$$

and the induced norm $\|u\|_{L^2(\Omega)} \doteq \|u\| := (u, u)^{1/2}$. For convenience, the same notation as in (8) will also be used for the integral of the product of two functions, even if these functions are not in $L^2(\Omega)$, and for both scalar and vector fields. The space of functions whose distributional derivatives up to order m belong to $L^2(\Omega)$ is denoted by $H^m(\Omega)$. In particular, $H^1(\Omega)$ is also a Hilbert space, and we will focus on this case.

The weak form of the fluid-structure interaction problem in free surface potential flow (7) reads: find $[\phi, \mathbf{u}] \in \mathcal{W} \times \mathcal{V}$ such that

$$a([\phi, \mathbf{u}], [w, \mathbf{v}]) = b([w, \mathbf{v}]) \qquad \forall [w, \mathbf{v}] \in \mathcal{W} \times \mathcal{V}, \tag{9}$$

where $\mathcal{W} \doteq H^1(\Omega)$ and $\mathcal{V} \doteq \mathbb{C}^d$ are a space of vectorial complex numbers of dimension d. In this case, since we consider translational motion only, d is equal to the topological dimension of the domain Ω. The bilinear and linear forms are defined as follows:

$$\begin{aligned} a([\phi, \mathbf{u}], [w, \mathbf{v}]) := (\nabla w, \nabla\phi)_\Omega - \frac{\omega^2}{g}(w, \phi)_{\Gamma_f} + i\omega\,(w, \mathbf{u}\cdot\boldsymbol{n}_\Gamma)_\Gamma + \\ - \omega^2 \frac{\boldsymbol{M}_\rho}{|\Gamma|}(\mathbf{v}, \mathbf{u})_\Gamma - i\omega\,(\mathbf{v}, \phi\boldsymbol{n}_\Gamma)_\Gamma + g\,(\mathbf{v}, (\boldsymbol{n}_z\cdot\mathbf{u})\,\boldsymbol{n}_\Gamma)_\Gamma\,, \end{aligned} \tag{10}$$

and

$$b([w, \mathbf{v}]) := (w, v_{in})_{\Gamma in} + (w, v_{out})_{\Gamma out}\,. \tag{11}$$

In equation (10), $\boldsymbol{M}_\rho$ is the relative mass with respect to the fluid density, i.e. $\boldsymbol{M}_\rho \doteq \frac{\boldsymbol{M}}{\rho}$. In the definitions of the bilinear form $a([\phi, \mathbf{u}], [w, \mathbf{v}])$ and the linear form $b([w, \mathbf{v}])$ in equations (10) and (11), the kinematic boundary conditions (7b)-(7f) are used. The last term in (10) enforces the dynamic interface condition (7g) between the fluid and solid, where the mass term is averaged over the boundary measure $|\Gamma| := \int_\Gamma d\Gamma$, assuming the mass is uniform over the body.

It is worth emphasizing that the formulation in (9) is tailored to structures with rigid body motions, but the same framework can be extended to elastic structures. Additionally, we assume a monolithic coupling between fluid and structure, meaning that both fluid and solid degrees of freedom are solved as part of a single coupled system of equations.

In this work we solve problem (9) using a FEM approach. Let us consider the Finite Element (FE) partition Ω_h of the domain Ω from which we can construct conforming finite dimensional spaces for the velocity potential $\mathcal{W}_h \subset \mathcal{W}$. Here we use the following definition for the velocity potential FE space

$$\mathcal{W}_h \doteq \left\{ w_h \in \mathcal{C}^0(\Omega_h) : w_h\,|_K \in \mathbb{P}^r(K), \forall K \in \Omega_h \right\}. \tag{12}$$

Where $\mathbb{P}^r(K)$ are the Lagrange polynomials of degree up to r in an element K. Note that the body motion is just a complex vector value $\mathbf{u} \in \mathbb{C}^d$, which could be understood as a vector type complex-valued constant FE space $\mathcal{V}_h \doteq \mathbb{C}^d$ over any given domain; in that case, it is sufficient to have $\mathcal{V}_h$ defined over Γ_h, which is the set of edges of Ω_h belonging to Γ. In this work a rigid body is considered, but the formulation can be extended to an elastic structure as described by Colomés et al. [14]. The estimation of hydrodynamic coefficients for elastic structures is considered out of the scope of this work.

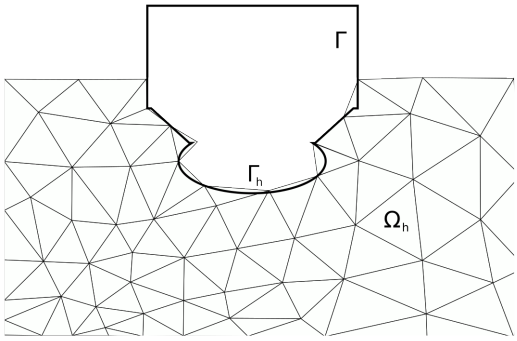

FIGURE 2. Reference conformal domain Ω_h with arbitrary shaped boundary Γ_h and true boundary Γ.

With these definitions, the discrete fluid-structure interaction problem in the frequency domain reads: find $[\phi_h, \mathbf{u}_h] \in \mathcal{W}_h \times \mathcal{V}_h$ such that

$$a_h([\phi_h, \mathbf{u}_h], [w_h, \mathbf{v}_h]) = b_h([w_h, \mathbf{v}_h]) \qquad \forall [w_h, \mathbf{v}_h] \in \mathcal{W}_h \times \mathcal{V}_h \tag{13}$$

Where a_h and b_h are the bilinear and linear forms defined in (10) and (11), respectively, with the corresponding discrete integration domains as depicted in Figure 2.

The discrete form (13) can be expressed in an equivalent matrix form as follows:

$$\begin{pmatrix} \mathbb{A}_{w\phi} & \mathbb{A}_{wu} \\ \mathbb{A}_{v\phi} & \mathbb{A}_{vu} + \mathbb{C}_{vu} \end{pmatrix} \begin{pmatrix} \boldsymbol{\Phi} \\ \boldsymbol{U} \end{pmatrix} = \begin{pmatrix} \boldsymbol{F}_\phi \\ \boldsymbol{F}_u \end{pmatrix}, \tag{14}$$

with

$$\mathbb{A}_{w\phi} \doteq (\nabla w_h, \nabla \phi_h)_{\Omega_h} - \frac{\omega^2}{g} (w_h, \phi_h)_{\Gamma_{f,h}}, \tag{15a}$$

$$\mathbb{A}_{wu} \doteq i\omega (w_h, \mathbf{u}_h \cdot \boldsymbol{n}_\Gamma)_{\Gamma_h}, \tag{15b}$$

$$\mathbb{A}_{v\phi} \doteq -i\omega (\mathbf{v}_h, \phi_h \boldsymbol{n}_\Gamma)_{\Gamma_h}, \tag{15c}$$

$$\mathbb{A}_{vu} \doteq -\omega^2 \frac{\boldsymbol{M}_\rho}{|\Gamma|} (\mathbf{v}_h, \mathbf{u}_h)_{\Gamma_h}, \tag{15d}$$

$$\mathbb{C}_{vu} \doteq g (\mathbf{v}_h, (\boldsymbol{n}_z \cdot \mathbf{u}_h) \boldsymbol{n}_\Gamma)_{\Gamma_h}, \tag{15e}$$

$$\boldsymbol{F}_\phi \doteq (w_h, u_{in})_{\Gamma in,h} + (w_h, u_{out})_{\Gamma out,h}, \tag{15f}$$

$$\boldsymbol{F}_u \doteq \mathbf{0}. \tag{15g}$$

In equation (14), $\boldsymbol{\Phi}$ is the vector of degrees of freedom associated to the discrete velocity potential, $\boldsymbol{U} \doteq \mathbf{u}_h$ is the complex-valued vector associated to the body

displacement. We use bold symbols to denote vectorial quantities and blackboard bold to denote matrices. Note that the matrices $\mathbb{A}_{vu}$ and $\mathbb{C}_{vu}$, and the vector $\boldsymbol{F}_u$ are of dimension $d \times d$ and $d \times 1$, respectively, with $d \leq 6$. As, in 2D, these terms consist of two translational and one rotational degree of freedom and, in 3D, there are three translational plus three rotational degrees of freedom allowed.

2.3. **Hydrodynamic coefficient estimation.** We can reduce the algebraic system (14) to a single equation, condensing the contribution from $\boldsymbol{\Phi}$, which leads to

$$\left(\mathbb{A}_{vu} + \mathbb{C}_{vu} - \mathbb{A}_{v\phi}\mathbb{A}_{w\phi}^{-1}\mathbb{A}_{wv}\right)\boldsymbol{U} = \boldsymbol{F}_u - \mathbb{A}_{v\phi}\mathbb{A}_{w\phi}^{-1}\boldsymbol{F}_\phi. \tag{16}$$

Here, equation (16) is equivalent to the equation of motion of a spring-mass-damper system with a single degree of freedom. The first term $\mathbb{A}_{vu}$ corresponds to the inertia term of the body, the second term $\mathbb{C}_{vu}$ corresponds to the spring stiffness given by the hydrostatic restoring force, and the third term $\mathbb{A}_{v\phi}\mathbb{A}_{w\phi}^{-1}\mathbb{A}_{wv}$ corresponds to the added inertia and damping experienced by the object due to the surrounding fluid. Therefore, we obtain the equation for added mass in (17) and the equation for added damping in (18).

$$\boldsymbol{A} = \frac{Re\left(\mathbb{A}_{v\phi}\mathbb{A}_{w\phi}^{-1}\mathbb{A}_{wv}\right)}{\omega^2} \tag{17}$$

$$\boldsymbol{B} = \frac{Im\left(\mathbb{A}_{v\phi}\mathbb{A}_{w\phi}^{-1}\mathbb{A}_{wv}\right)}{\omega} \tag{18}$$

The non-dimensionalized added mass and added damping are stated in (19) and (20) respectively, given density ρ and submerged area $\forall$.

$$\bar{\boldsymbol{A}} = \frac{\boldsymbol{A}}{\rho\forall} \tag{19}$$

$$\bar{\boldsymbol{B}} = \frac{\boldsymbol{B}}{\omega\rho\forall} \tag{20}$$

3. **Unfitted Finite Element methods.** In this work, we consider three types of unfitted FE methods, namely the Aggregated Unfitted Finite Element Method (AgFEM) [8], Cut Finite Element Method (CutFEM) [20], and the Shifted Boundary Method (SBM)[26]. Generally, unfitted FE methods have the following challenges: imposition of boundary conditions, integration of cut cells, and matrix conditioning with regard to small cut cells. Each of the aforementioned unfitted FE methods addresses these challenges in their own way. We refer the reader to the mentioned works for a detailed description of the respective methods. In this work, we briefly describe how each method is applied in what concerns the hydrodynamic coefficient estimation. However, before introducing the unfitted FE methods, the domains are introduced and some remarks on common definitions are described.

3.1. **Domain definitions.** The unfitted methods discussed in this work have varying definitions and terminology for the domains and boundaries of interest, which are introduced and defined in this section.

Here, we will distinguish between four triangulations, namely: physical, cut, active, and surrogate domain or boundary. Physical triangulation corresponds to a triangulation composed by active elements of the non-conforming background grid where the cut elements are tesselated to generate conforming triangulation to the

boundary Γ, which is depicted in Figure 3 with the cut cells highlighted in red. The physical triangulation can be understood as a conformal triangulation. Since the number of tessellations on cut cells can be arbitrarily large, it is often only used for integration purposes. Note that here we do not discuss how to tesselate the cut elements; see details in [5] and references therein. The cut domain Ω_h^{cut} consists of all cells which have an intersection with the physical boundary Γ_h. The surrogate domain $\tilde{\Omega}_h$ corresponds to all cells which are in the physical domain, but are *not* cut cells. The active domain Ω_h^{act} corresponds to all cells, which are either cut or in the physical domain and thus $\Omega_h^{\text{act}} = \Omega_h^{\text{cut}} \cup \tilde{\Omega}_h$, see Figure 4.

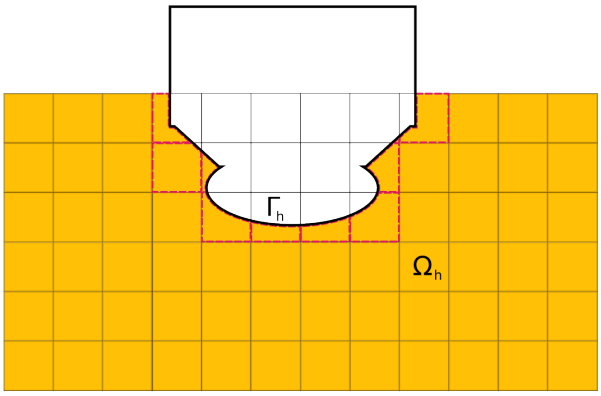

FIGURE 3. Definitions of the physical domain Ω_h (yellow) with arbitrary shaped boundary Γ_h. The red dashed outline highlights the cells that are constructed using special numerical integration rules.

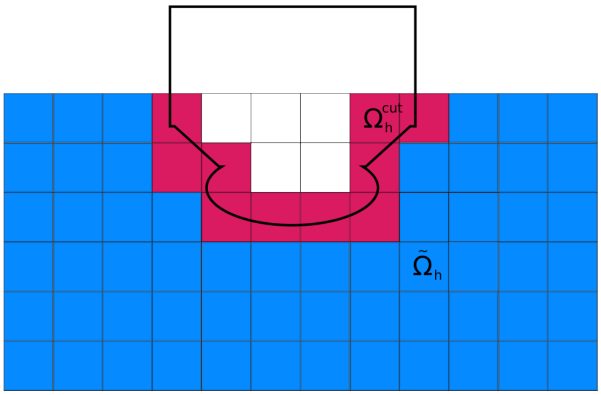

FIGURE 4. Definitions of the surrogate $\tilde{\Omega}_h$ (blue), cut Ω_h^{cut} (red) and active Ω_h^{act} (both blue and red) domains.

3.2. **Aggregated unfitted finite element method.** The core principle of AgFEM is to construct a FE space using a discrete extension operator. This operator extends the FE functions defined on interior cells to the cut cells. The process involves a cell aggregation approach, where the exterior degrees of freedom, i.e. the degrees of freedom outside the domain Ω associated with cut cells, are constrained by those of the interior cells to which they are aggregated. As a result, exterior degrees of freedom are eliminated and the algebraic linear system is dependent only on interior degrees of freedom, effectively avoiding ill-conditioning associated with small cut cells. Briefly summarizing, an exterior degree of freedom is associated with an interior cell via a cell aggregation scheme, and the value of the exterior degree of freedom is then computed via extrapolation of a number of the degrees of freedom within that associated interior cell. The cell aggregation algorithm is set to aggregate all cut cells to interior cells. Alternatively, it is possible to relax this constraint by aggregating only small cut cells by applying some threshold dependent on the ratio of the cut cell volume w.r.t. background cell volume. A detailed discussion of the methodology and mathematical foundations of AgFEM is beyond the scope of this work; interested readers are directed to [8] for further information.

For AgFEM, we require to enhance the FE space with the cell aggregation technique, while integration is carried out in the physical triangulation. The AgFEM FE space is given by

$$\mathcal{W}_h^{\mathrm{ag}} \doteq \left\{ w_h \in \mathcal{C}^0(\Omega_h^{\mathrm{act}}) : w_h \mid_A \in \mathbb{P}^r(A), \forall A \in \Omega_h^{\mathrm{act}} \right\}, \tag{21}$$

where, abusing notation, A are the cell aggregates. The resulting weak form is similar to that of the conformal case: find $[\phi_h, \mathbf{u}_h] \in \mathcal{W}_h^{\mathrm{ag}} \times \mathcal{V}_h$ such that

$$a_h^{\mathrm{ag}}([\phi_h, \mathbf{u}_h], [w_h, \mathbf{v}_h]) = b_h([w_h, \mathbf{v}_h]) \qquad \forall [w_h, \mathbf{v}_h] \in \mathcal{W}_h^{\mathrm{ag}} \times \mathcal{V}_h \tag{22}$$

noting that $\mathcal{W}_h^{\mathrm{ag}}$ is the enhanced FE space. The bilinear and linear forms remain the same as defined in equations (10) and (11), respectively. It should be noted here that the integration triangulations appearing in these equations, Ω_h, $\Gamma_{f,h}$ and Γ_h, are obtained via cut cell integration and thus differ from the conformal case.

For the estimation of hydrodynamic coefficients the required terms from the weak form as defined in (15) for the conformal case are equivalent to the AgFEM approach, denoting that the integration terms are now obtained via cut cell integration. Therefore, for the AgFEM method, the only modification required to obtain the hydrodynamic coefficients with respect to the conformal case is the definition of the aggregated finite element spaces.

3.3. **Cut finite element method.** In CutFEM, the FE spaces are defined in the active triangulation, and integration is applied in the physical triangulation. In order to address instabilities arising from small cut cells and the accompanied matrix ill-conditioning, ghost penalty stabilization is applied [11]. The weak form is: find $[\phi_h, \mathbf{u}_h] \in \mathcal{W}_h^{\mathrm{act}} \times \mathcal{V}_h$ such that

$$a_h^{\mathrm{cut}}([\phi_h, \mathbf{u}_h], [w_h, \mathbf{v}_h]) = b_h([w_h, \mathbf{v}_h]) \qquad \forall [w_h, \mathbf{v}_h] \in \mathcal{W}_h^{\mathrm{act}} \times \mathcal{V}_h, \tag{23}$$

with the bilinear form defined as:

$$\begin{aligned} a_h^{\mathrm{cut}}([\phi_h, \mathbf{u}_h], [w_h, \mathbf{v}_h]) :=& a_h([\phi_h, \mathbf{u}_h], [w_h, \mathbf{v}_h]) \\ &+ \sum_{i=1}^{p} \langle [\![\nabla^{(i)} w_h \cdot \boldsymbol{n}_{\mathcal{T}_G}]\!], \gamma {h_e}^{(2i+1)} [\![\nabla^{(i)} \phi_h \cdot \boldsymbol{n}_{\mathcal{T}_G}]\!] \rangle_{\mathcal{T}_G}. \end{aligned} \tag{24}$$

Here, the ghost penalty stabilization term is dependent on the order p, an algorithmic constant $\gamma > 0$, which in this work is taken to be $\gamma = 0.1$ and characteristic cell size length scale h_e. The linear form is as given in (11).

For the estimation of hydrodynamic coefficients, we have to modify the system of equations to:

$$\begin{pmatrix} \mathbb{A}_{w\phi} + \mathbb{E}_{w\phi} & \mathbb{A}_{wu} \\ \mathbb{A}_{v\phi} & \mathbb{A}_{vu} + \mathbb{C}_{vu} \end{pmatrix} \begin{pmatrix} \boldsymbol{\Phi} \\ \boldsymbol{U} \end{pmatrix} = \begin{pmatrix} \boldsymbol{F}_{\phi} \\ \boldsymbol{F}_{u} \end{pmatrix}, \tag{25}$$

with all terms except $\mathbb{E}_{w\phi}$ to be defined in the set of equations (15) and $\mathbb{E}_{w\phi}$ defined in (26).

$$\mathbb{E}_{w\phi} \doteq \sum_{i=1}^{p} \langle [\![\nabla^{(i)} w_h \cdot \boldsymbol{n}_{\mathcal{T}_G}]\!], \gamma {h_e}^{(2i+1)} [\![\nabla^{(i)} \phi_h \cdot \boldsymbol{n}_{\mathcal{T}_G}]\!] \rangle_{\mathcal{T}_G}. \tag{26}$$

It is important to highlight that the problem of interest, equation (7), is a pure Neumann-type problem. In this case, the additional term defined in (26) is not required for stability purposes, but is required to prevent ill-conditioning of the system [20, 16]. In this work, we assess what the influence is in the estimation of hydrodynamic coefficients when adding the ghost penalty term, see Section 4.1.

3.4. **Shifted Boundary Method.** The SBM uniquely differs from the aforementioned methods by completely avoiding cell cutting. SBM requires only the non-cut cells and uses a Taylor series expansion to approximate the physical boundary condition on the surrogate boundary. At the basis of this method lies the map $\mathcal{M}$ that maps points from the surrogate boundary to the true boundary:

$$\begin{aligned} \mathcal{M} : \tilde{\Gamma} &\longrightarrow \Gamma \\ \tilde{\mathbf{x}} &\longrightarrow \mathcal{M}(\tilde{\mathbf{x}}) = \mathbf{x} = \mathbf{d} + \tilde{\mathbf{x}}. \end{aligned} \tag{27}$$

Where $\mathbf{d} \doteq \mathbf{x} - \tilde{\mathbf{x}}$ is a distance vector that could be obtained, for example, through closest point projection algorithms. Then, any function evaluated at the true boundary, Γ, can be approximated by a Taylor series expansion, in that case truncated after the second term, evaluated at the surrogate boundary, $\tilde{\Gamma}$:

$$f(\mathbf{x}) = f(\mathcal{M}(\tilde{\mathbf{x}})) = f(\tilde{\mathbf{x}}) + \nabla f(\tilde{\boldsymbol{x}})\mathbf{d} + \mathcal{O}(\mathbf{d}^2). \tag{28}$$

The Neumann-type boundary is shifted using an approach similar to [4]. Thereby, we introduce three additional terms to the weak form corresponding to the decomposition of the flux along the true normal and tangential directions. Additionally, the dynamic boundary condition is modified, as this is defined using the integral on the physical boundary. In order to address the change in area between the surrogate and true boundary, we require a Jacobian operator $J = \det(\boldsymbol{I} + \nabla \boldsymbol{d})$ with $\boldsymbol{I}$ the identity matrix. In the hydrodynamic pressure term, the velocity potential is only defined on the surrogate boundary and has to be shifted as well, whereas the displacement of a rigid object does not have to be shifted. As a result, the weak form for the SBM method reads: find $[\phi_h, \mathbf{u}_h] \in \mathcal{W}_h^{\text{sbm}} \times \mathcal{V}_h$ such that

$$a_h^{\text{sbm}}([\phi_h, \mathbf{u}_h], [w_h, \mathbf{v}_h]) = b_h([w_h, \mathbf{v}_h]) \qquad \forall [w_h, \mathbf{v}_h] \in \mathcal{W}_h^{\text{sbm}} \times \mathcal{V}_h, \tag{29}$$

with the bilinear form given by:

$$\begin{aligned} a_h^{\text{sbm}}([\phi_h, \mathbf{u}_h], [w_h, \mathbf{v}_h]) := (\nabla w_h, \nabla \phi_h)_{\tilde{\Omega}_h} - \frac{\omega^2}{g} (w_h, \phi_h)_{\tilde{\Gamma}_{f,h}} \\ - \omega^2 \frac{\boldsymbol{M}_{\rho}}{\left|\tilde{\Gamma}_h\right|} (\mathbf{v}_h, \mathbf{u}_h)_{\tilde{\Gamma}_h} + gJ \left(\mathbf{v}_h, \mathbf{u}_h \left(\boldsymbol{n}_z \cdot (\boldsymbol{n}_{\Gamma} \cdot \tilde{\boldsymbol{n}}_{\Gamma}) \boldsymbol{n}_{\Gamma}\right)\right)_{\tilde{\Gamma}_h} \end{aligned} \tag{30}$$

$$
\begin{aligned}
&- i\omega J\left(\mathbf{v}_h, (\phi_h + \nabla\phi_h \cdot \mathbf{d})(\boldsymbol{n}_\Gamma \cdot \tilde{\boldsymbol{n}}_\Gamma)\boldsymbol{n}_\Gamma\right)_{\tilde{\Gamma}_h} \\
&- \left(w_h, \nabla\phi_h \cdot \tilde{\boldsymbol{n}}_\Gamma\right)_{\tilde{\Gamma}_h} - i\omega\left(w_h, \mathbf{u}_h \cdot (\boldsymbol{n}_\Gamma \cdot \tilde{\boldsymbol{n}}_\Gamma)\boldsymbol{n}_\Gamma\right)_{\tilde{\Gamma}_h} \\
&+ \left(w_h, (\boldsymbol{n}_\Gamma \cdot \tilde{\boldsymbol{n}}_\Gamma)\boldsymbol{n}_\Gamma \cdot (\nabla(\nabla\phi_h) \cdot \mathbf{d} + \nabla\phi_h)\right)_{\tilde{\Gamma}_h},
\end{aligned}
$$

and the SBM FE space $\mathcal{W}_h^{\text{sbm}}$ defined as

$$
\mathcal{W}_h^{\text{sbm}} \doteq \left\{ w_h \in \mathcal{C}^0(\tilde{\Omega}_h) : w_h \mid_K \in \mathbb{P}^r(K), \forall K \in \tilde{\Omega}_h \right\}. \tag{31}
$$

Note that for the SBM method with Neumann-type boundaries, the Taylor expansion is applied to the gradient, which will introduce one order loss to the error convergence. Additionally, if linear elements are used to construct the FE space $\mathcal{W}_h^{\text{sbm}}$, the expansion vanishes. However, in the latter case, there is still improvement in the solution compared to the equivalent conformal case in $\tilde{\Omega}_h$ due to the effect of the correction introduced by the normal product $(\boldsymbol{n}_\Gamma \cdot \tilde{\boldsymbol{n}}_\Gamma)\boldsymbol{n}_\Gamma$. The loss of order in SBM for Neumann-type boundary conditions can be avoided by solving a mixed problem on a layer of elements attached to the surrogate boundary, as proposed in [4]. The implementation of this correction is considered out of the scope of this study and will be carried out in a follow-up work.

The discrete form (29) can be expressed in an equivalent matrix form as follows:

$$
\begin{pmatrix} \tilde{\mathbb{A}}_{w\phi} & \tilde{\mathbb{A}}_{wu} \\ \tilde{\mathbb{A}}_{v\phi} & \tilde{\mathbb{A}}_{vu} + \tilde{\mathbb{C}}_{vu} \end{pmatrix} \begin{pmatrix} \boldsymbol{\Phi} \\ \boldsymbol{U} \end{pmatrix} = \begin{pmatrix} \boldsymbol{F}_\phi \\ \boldsymbol{F}_u \end{pmatrix}, \tag{32}
$$

with

$$
\tilde{\mathbb{A}}_{w\phi} \doteq (\nabla w_h, \nabla\phi_h)_{\tilde{\Omega}_h} - \frac{\omega^2}{g}\left(w_h, \phi_h\right)_{\tilde{\Gamma}_{f,h}}, \tag{33a}
$$

$$
\tilde{\mathbb{A}}_{wu} \doteq i\omega\left(w_h, \mathbf{u}_h \cdot (\boldsymbol{n}_\Gamma \cdot \tilde{\boldsymbol{n}}_\Gamma)\boldsymbol{n}_\Gamma\right)_{\tilde{\Gamma}_h}, \tag{33b}
$$

$$
\tilde{\mathbb{A}}_{v\phi} \doteq -i\omega J\left(\mathbf{v}_h, (\phi_h + \nabla\phi_h \cdot \mathbf{d})(\boldsymbol{n}_\Gamma \cdot \tilde{\boldsymbol{n}}_\Gamma)\boldsymbol{n}_\Gamma\right)_{\tilde{\Gamma}_h}, \tag{33c}
$$

$$
\tilde{\mathbb{A}}_{vu} \doteq -\omega^2 \frac{\boldsymbol{M}_\rho}{\left|\tilde{\Gamma}_h\right|}\left(\mathbf{v}_h, \mathbf{u}_h\right)_{\tilde{\Gamma}_h}, \tag{33d}
$$

$$
\tilde{\mathbb{C}}_{vu} \doteq gJ\left(\mathbf{v}_h, \mathbf{u}_h\left(\boldsymbol{n}_z \cdot (\boldsymbol{n}_\Gamma \cdot \tilde{\boldsymbol{n}}_\Gamma)\boldsymbol{n}_\Gamma\right)\right)_{\tilde{\Gamma}_h}. \tag{33e}
$$

The equations for estimation of the hydrodynamic coefficients then take the following form:

$$
\bar{\boldsymbol{A}} = \frac{Re\left(\tilde{\mathbb{A}}_{v\phi}\tilde{\mathbb{A}}_{w\phi}^{-1}\tilde{\mathbb{A}}_{wv}\right)}{\omega^2\rho\forall} \tag{34}
$$

$$
\bar{\boldsymbol{B}} = \frac{Im\left(\tilde{\mathbb{A}}_{v\phi}\tilde{\mathbb{A}}_{w\phi}^{-1}\tilde{\mathbb{A}}_{wv}\right)}{\omega^2\rho\forall} \tag{35}
$$

4. **Case studies.** We assess the unfitted FE methods, by comparing their accuracy on several experiments in 2D. The first study is a sensitivity analysis on the ghost penalty parameter γ. The second study is derived from experimental work on several surface-piercing geometries by Vugts [34], and the third study focuses on the estimation of the added mass and the added damping of a horizontal cylinder at varying submergence depths, based on the work by Greenhow et al. [19]. In the former case, novel numerical methods have been tested, i.e. a Harmonic Polynomial Cell (HPC) approach by Liang et al. [23] and an Extended FE method (XFEM)

by Wang et al. [36]. Lastly, the condition number across the previous two studies is compared.

Historically, the case studies considered in this work have been conducted analytically with infinite domain lengths. In this work, we apply the radiation condition at the matching boundaries that are sufficiently far from the object of interest as done by Wang et al. [36]. Due to the symmetry of the geometries in this study, we consider only the right half of the fluid domain and enforce the horizontal fluid velocity to be zero in the symmetry plane. The symmetry plane corresponds to the inlet boundary, and the matching boundary corresponds to the outlet boundary. Therefore, we rewrite the boundary conditions on the inlet and outlet boundaries to:

$$\nabla\phi \cdot \boldsymbol{n}_{in} = 0 \quad \text{on} \quad \Gamma_{in} \tag{36}$$

$$\nabla\phi \cdot \boldsymbol{n}_{out} = ik\phi \quad \text{on} \quad \Gamma_{out}. \tag{37}$$

Note that in equation (37), the boundary condition depends on the solution; thus, the equivalent term will go into the matrix $\mathbb{A}_{w\phi}$ instead of the right-hand side of the system.

In Figure 5 a generalised overview of the boundaries and domain parameters is presented that is applicable to all case studies conducted. In each case study, the geometric boundary Γ, highlighted in red, will differ. On the top is the free surface Γ_f, on the right is the outlet Γ_{out}, on the bottom is the seabed Γ_{sb}, and on the bottom left is the inlet Γ_{in}. The domain parameters are: distance of submergence H, domain length L_x, and depth d.

The length of the domain L_x should be sufficiently large for the matching boundary, Wang et al. [36] studied the effect of varying ratios of domain length L_x over the longest wavelength λ_{max}, and states that $L_x/\lambda_{max} \geq 1.0$ is sufficient for a given smallest non-dimensional wave number $\bar{k} = 0.1$.

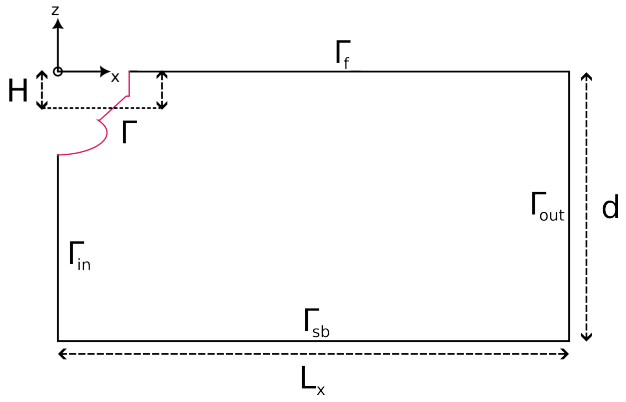

FIGURE 5. Overview of boundaries and domain size parameters.

Notes on implementation. This work has been conducted using the software package *Gridap.jl* and sub-packages *GridapGmsh.jl* and *GridapEmbedded.jl* [31] [7], and the *GMSH* meshing software [18]. Gridap is an open-source FE toolbox written in the Julia programming language [9]. The background meshes for this study are built in *GMSH* and loaded using the sub-package *GridapGmsh.jl*. The cell cutting

algorithm and the cell aggregation scheme are the default approach for analytical geometries as defined in the *GridapEmbedded.jl* package via level set. We used the functionalities of this sub-package to generate the required domains for SBM, as this is currently not a feature of this sub-package.

4.1. **Ghost penalty for Neumann-type boundary - heaving cylinder.** For the case of purely Neumann-type boundary conditions, the ghost penalty stabilization terms might not be required. Therefore, an initial study is conducted for CutFEM. Two cases are considered: one neglecting the ghost penalty stabilization terms and one including these stabilization terms, and varying the parameter γ. The effect of these variations on the condition number via the L1 norm is studied for increasing number of elements n and for varying submergence depth H. The geometry considered is a horizontal cylinder and the submergence depth is varied to enforce the creation of small cut cells. The mesh considered here is a Cartesian grid with n number of elements, due to the rectangular domain setup the number of elements is set to $(3n, n)$ for x and z direction respectively.

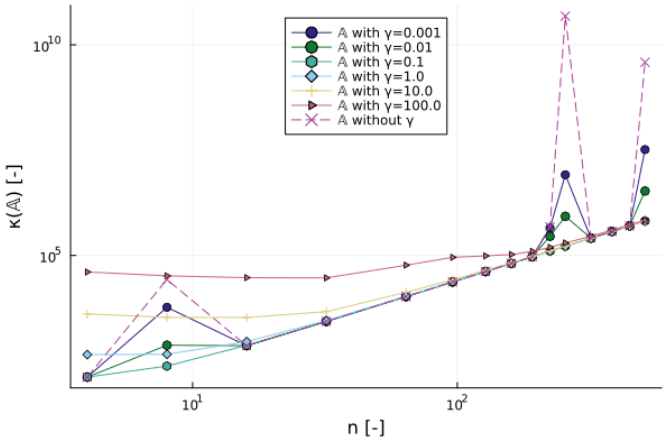

FIGURE 6. The condition number $\kappa(\mathbb{A})$ for varying number of elements n between a CutFEM approach with varying ghost penalty parameters and one without ghost penalty stabilization.

In Figure 6 the number of elements n is plotted against the condition number $\kappa(\mathbb{A})$, indicating that the ghost penalty effectively reduces the condition number for certain cases, presumably the ones with smaller cut cells. The larger stabilization parameters $\gamma > 1.0$ appear to introduce larger condition numbers in general. Especially for a lower number of elements, but also for a higher number of elements these parameters correspond to a larger condition number, albeit that the difference is smaller. The smaller stabilization parameters $\gamma < 0.1$ are more prone to the ill-conditioning from small cut cells. From Figure 6 it is deduced that $\gamma = 0.1$ and $\gamma = 1.0$ perform optimally. In Figure 7 we show the condition number for varying the submergence distances for the case of $n = 128$. Ideally, if the submergence distance approximates a multiple of the cell length scale, we should see relatively larger condition numbers. This is visible at the five peaks in Figure 7. The smaller stabilization parameters are more prone to ill-conditioning, as is highlighted in Figure 8. Again, for the larger stabilization parameters there appears to

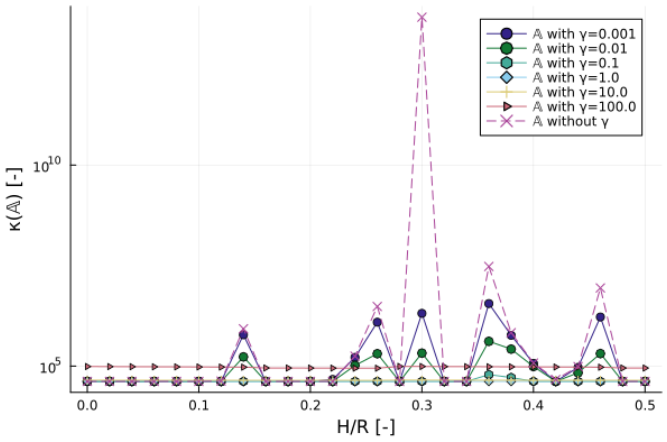

FIGURE 7. The condition number $\kappa(\mathbb{A})$ for varying submergence depth ratios H/R between a CutFEM approach with ghost penalty parameters and one without ghost penalty parameters.

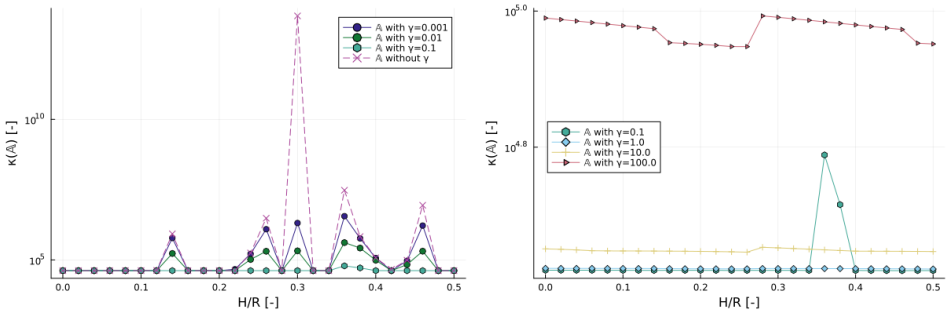

FIGURE 8. The condition number $\kappa(\mathbb{A})$ for varying submergence depth ratios H/R with a close up view on the smaller (left) and larger (right) ghost penalty parameters γ.

be no ill-conditioning, but generally there is a larger condition number, which is highlighted in Figure 8.

This study confirms that the ghost penalty stabilization is required to avoid ill-conditioning of the matrix, and it indicates that the original stabilization penalty parameter $\gamma = 0.1$ is sufficient for the cases considered in this work.

4.2. **Heaving rectangle.** We consider a two-dimensional surface-piercing rectangle with draft D and breadth B. We consider the same geometrical case setup as conducted by Wang et al. [36] and Liang et al. [23] The considered draft over breadth ratio is $D/B = 2$, and the domain dimensions are: depth $d = 40D$, and length $L_x = 2\lambda_{max}$ for a smallest non-dimensional wave number $\bar{k} = 0.1$. No variations in the distance of submergence are considered here and thus $H = 0.0$.

In Figure 9 we depict the mesh used to compute the hydrodynamic coefficients using the different methods described in Section 3. Note that the background

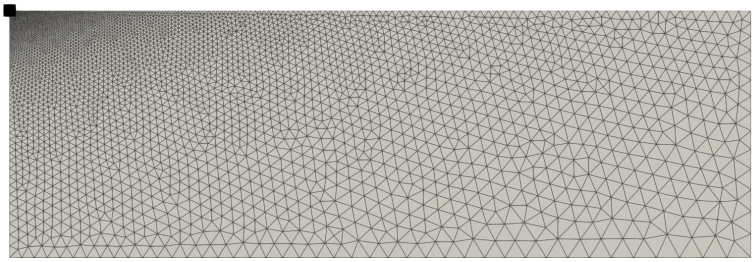

FIGURE 9. Background mesh for the heaving rectangle.

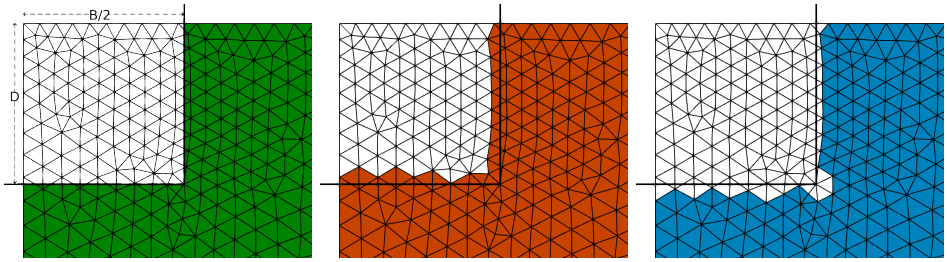

FIGURE 10. Close up view of the heaving rectange triangulations: physical triangulation, i.e. integration domain for AgFEM and CutFEM (left), active triangulation used by AgFEM and CutFEM (center) and surrogate triangulation used for the SBM (right).

mesh is refined towards the location of the embedded object, but the mesh is not conformal to the rectangle. In Figure 10 a close-up view of the triangulations for the heaving rectangle is displayed. The integration domain for AgFEM and CutFEM is displayed on the left, the active domain, which is used to generate the FE spaces for both AgFEM and CutFEM, is displayed in the middle, and on the right, the surrogate domain is displayed, which is used for both integration and generation of the FE space for the SBM method.

4.2.1. *Validation study.* The validation study is conducted for both linear and quadratic element types. For linear elements, the mesh consists of 48105 elements, while for quadratic elements, the mesh consists of 8217 elements. The results are depicted in Figure 11 and Figure 12 for linear and quadratic element types.

All unfitted FE methods follow the general trend dictated by the reference methods. For the added damping, the results agree well; the differences are more noticeable for the added mass coefficient. One general observation appears to be that the SBM is a visible outlier in this scenario. For SBM with order $p = 1$, we anticipate a difference due to the missing gradient recovery approach. For SBM $p = 2$, we see that the results match more accurately, indicating the correct shifting of the gradient. However, for SBM $p = 2$ the added damping coefficient is more underestimated than for SBM $p = 1$, although the differences with the other methods

are small. For AgFEM $p = 1$ and CutFEM $p = 1$, the added mass appears to be slightly underestimated, but it becomes indistinguishable for $p = 2$.

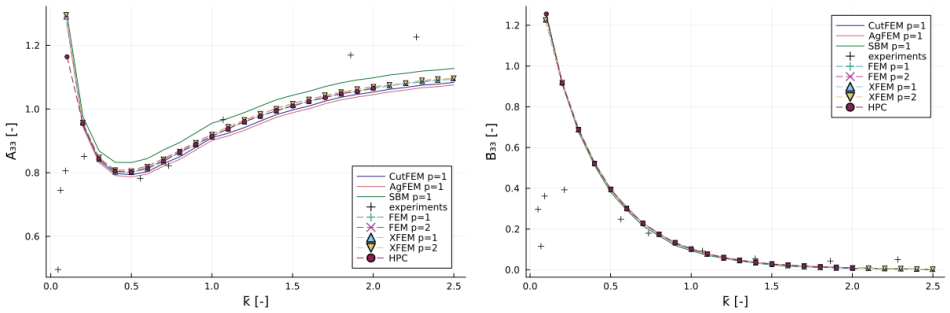

FIGURE 11. Non-dimensional wave number $\bar{k}$ versus non-dimensional added mass $\bar{A}_{33}$ and added damping $\bar{B}_{33}$ for elements of order $p = 1$ with reference data from [36] [23] [34].

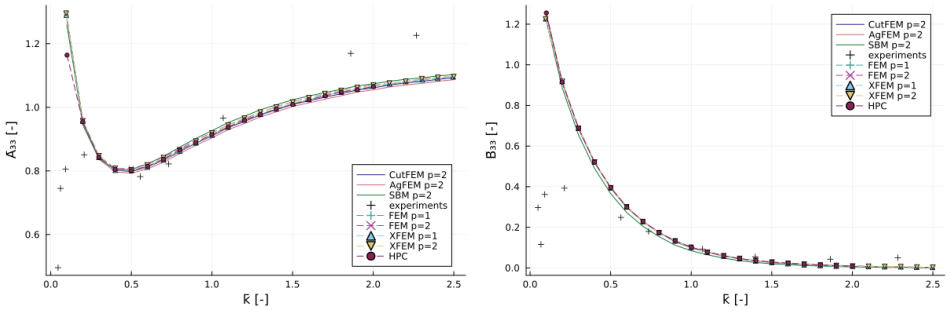

FIGURE 12. Non-dimensional wave number $\bar{k}$ versus non-dimensional added mass $\bar{A}_{33}$ and added damping $\bar{B}_{33}$ for elements of order $p = 2$ with reference data from [36] [23] [34].

4.3. **Horizontal cylinder.** We consider a two-dimensional surface-piercing horizontal cylinder of radius R. The domain dimensions are: depth $d = 20R$, and length $L_x = \lambda_{max}$. We determine λ_{max} using the non-dimensional wave number $\bar{k} = 0.15$. The horizontal cylinder is partially submerged to the submergence distance H using the following ratios of submergence depth over radius $H/R = 0.0, 0.342, 0.643, 0.809$, and 0.906. The submerged surface area $\forall$ is set as the full surface area of the cylinder in our computational domain, and thus $\forall = \pi R^2/2$. An immediate advantage of the unfitted FE methods to take note of is that we only require one single background mesh for all submerged cases. In Figure 13 we show the mesh used for the study of the partially submerged cylinder. As in the previous section, the mesh is refined towards the body, increasing accuracy without having to generate a body-fitted grid. A close-up view of the background mesh together with the physical, active, and surrogate triangulations is depicted in Figure 14.

In Figure 15 four close-up views of the meshes are depicted for varying depths of submergence for the horizontal cylinder, highlighting the surrogate domain used in

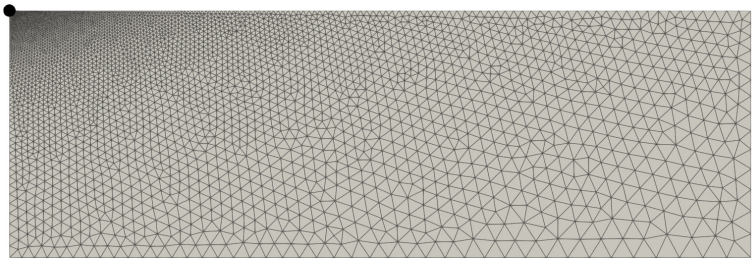

FIGURE 13. Background mesh for the submerged cylinder.

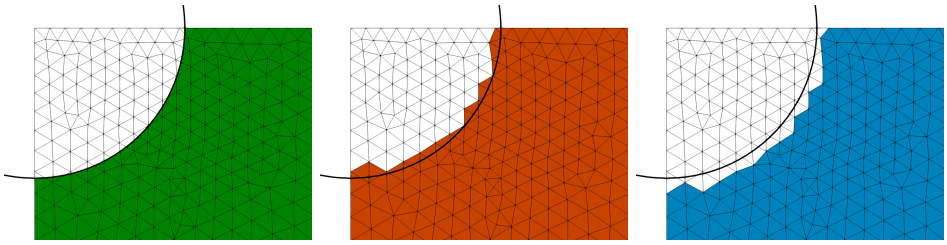

FIGURE 14. Close up view of the submerged cylinder triangulations for the case $H/R = 0.0$: physical triangulation, i.e. integration domain for AgFEM and CutFEM (left), active triangulation used by AgFEM and CutFEM (center) and surrogate triangulation used for the SBM (right).

the SBM method. Note that in this figure the mesh is used for illustration purposes; a higher resolution mesh is used for the calculations in this section. For $p = 1$ the mesh has 449485 elements and for $p = 2$ the mesh has 162203 elements.

4.3.1. *Validation study.* The reference data consists of an analytical approach for added mass and added damping, which is called the Relative Motion Hypothesis (RMH) combined with the Hasking relation for a symmetric two-dimensional body in vertical symmetry and asymptotic consequences of the Kramers-Kronig relation (see section 2 of [19] for the full formulation). For the smaller submergence depths this analytical approach approximates well, but for the larger submergence depths this method breaks down at the higher wave numbers. This is because of the assumption that the water plane length is equal to that of the case $H/R = 0.0$ for all submergence depths [19]. For the added damping an additional analytical formulation is presented, namely the Equivalent Wavemaker Theory (EWT). This approach replaces the structure by a wavemaker replicating the fluid velocity field generated by a high-frequency structure oscillation. The performance of this method should be better for the full range of wave numbers, although it is noted that for the increasing submergence depths this method breaks down in the intermediate wave number range and only sufficiently approximates the added damping for low wave numbers and wave numbers approximating infinity [19]. There is little experimental

and numerical data for the case of varying submergence depths. More often studies are focused on the effect of varying the domain depth for surface-piercing structures, i.e., deep to shallow water effects.

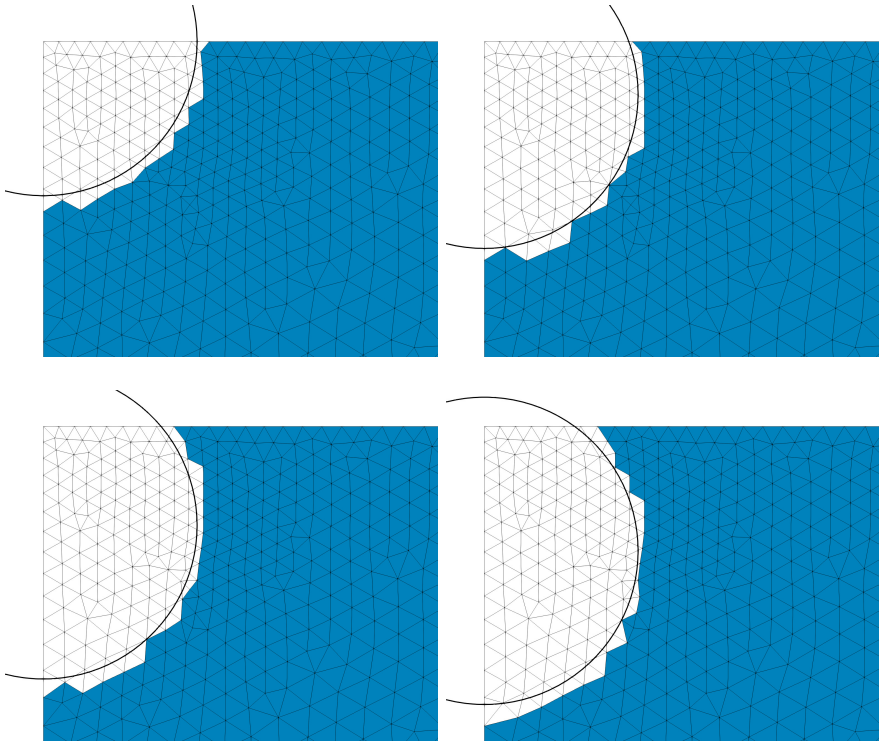

FIGURE 15. Close up view of the submerged cylinder triangulations for the cases $H/R = 0.0$ (top left), $H/R = 0.342$ (top right), $H/R = 0.643$ (bottom left) and $H/R = 0.809$ (bottom right).

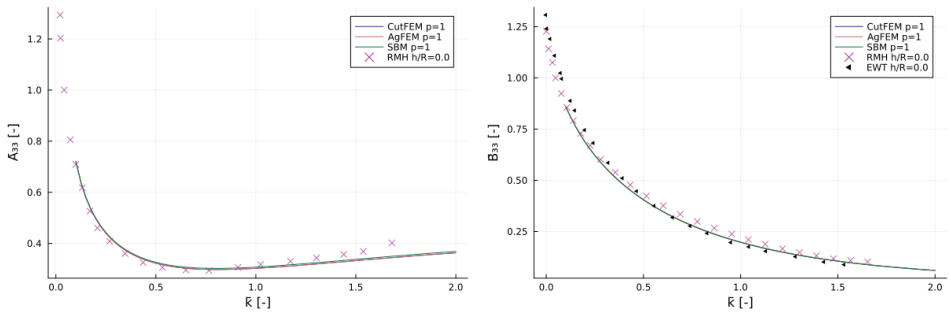

FIGURE 16. Non-dimensional wave number $\bar{k}$ versus non-dimensional added mass $\bar{A}_{33}$ and added damping $\bar{B}_{33}$ for submergence distance $H/R = 0.0$ with reference data from [19].

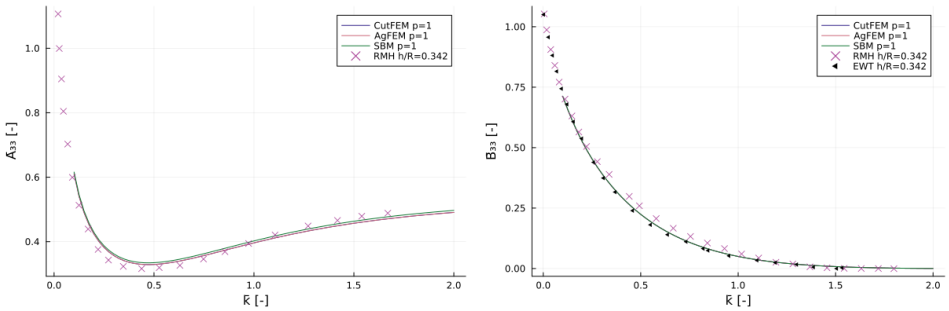

FIGURE 17. Non-dimensional wave number $\bar{k}$ versus non-dimensional added mass $\bar{A}_{33}$ and added damping $\bar{B}_{33}$ for submergence distance $H/R = 0.342$ with reference data from [19].

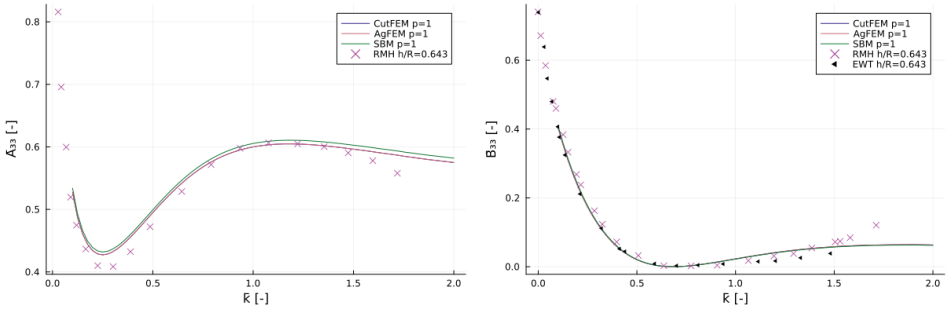

FIGURE 18. Non-dimensional wave number $\bar{k}$ versus non-dimensional added mass $\bar{A}_{33}$ and added damping $\bar{B}_{33}$ for submergence distance $H/R = 0.643$ with reference data from [19].

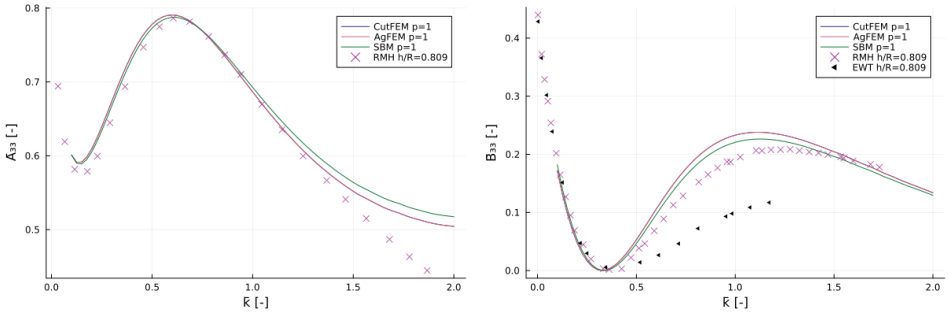

FIGURE 19. Non-dimensional wave number $\bar{k}$ versus non-dimensional added mass $\bar{A}_{33}$ and added damping $\bar{B}_{33}$ for submergence distance $H/R = 0.809$ with reference data from [19].

The results of this case study are depicted in Figure 16-20 for Lagrangian type elements of order $p = 1$, each plot depicting non-dimensional wave number versus

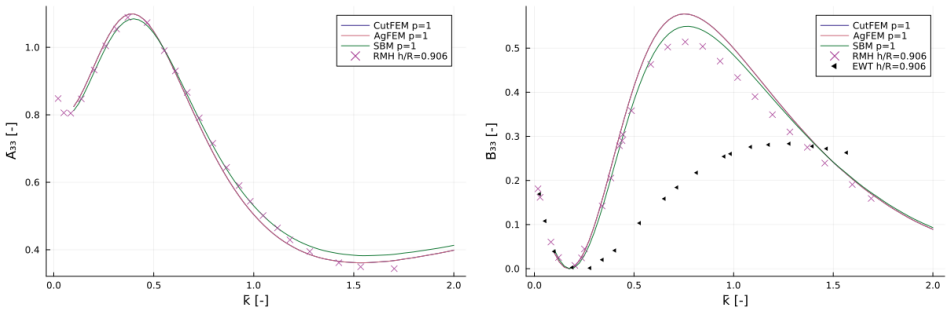

FIGURE 20. Non-dimensional wave number $\bar{k}$ versus non-dimensional added mass $\bar{A}_{33}$ and added damping $\bar{B}_{33}$ for submergence distance $h/R = 0.906$ with reference data from [19].

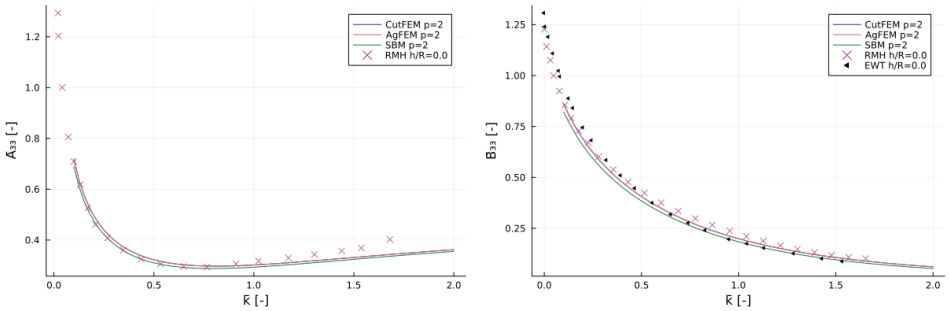

FIGURE 21. Non-dimensional wave number $\bar{k}$ versus non-dimensional added mass $\bar{A}_{33}$ and added damping $\bar{B}_{33}$ for submergence distance $H/R = 0.0$ with reference data from [19].

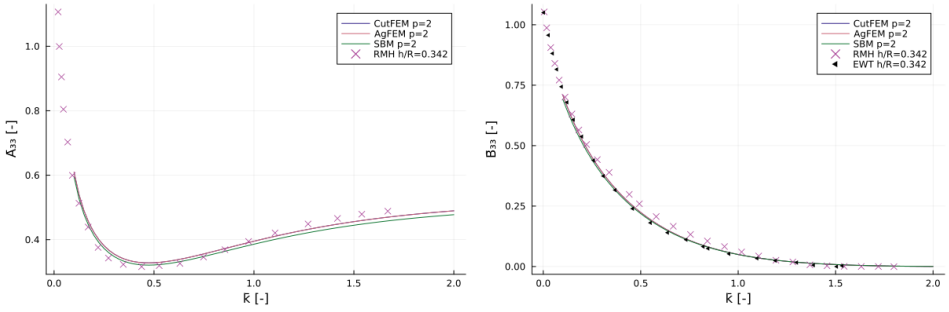

FIGURE 22. Non-dimensional wave number $\bar{k}$ versus non-dimensional added mass $\bar{A}_{33}$ and added damping $\bar{B}_{33}$ for submergence distance $H/R = 0.342$ with reference data from [19].

the added mass and added damping at increasing submergence depths. For elements

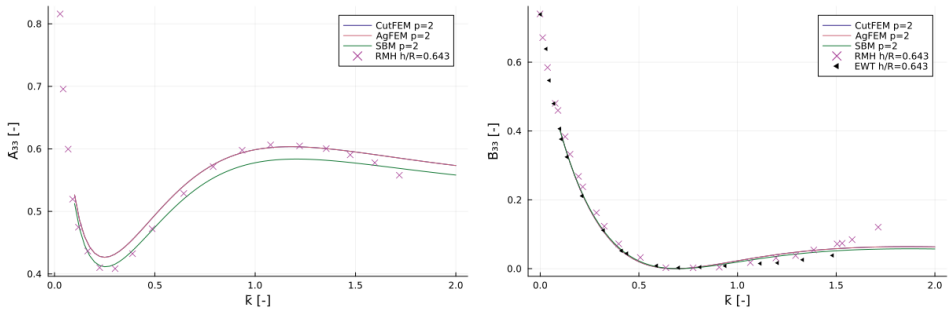

FIGURE 23. Non-dimensional wave number $\bar{k}$ versus non-dimensional added mass $\bar{A}_{33}$ and added damping $\bar{B}_{33}$ for submergence distance $H/R = 0.643$ with reference data from [19].

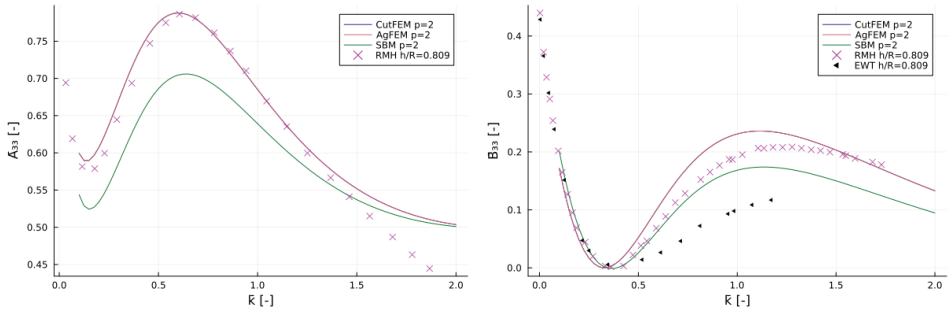

FIGURE 24. Non-dimensional wave number $\bar{k}$ versus non-dimensional added mass $\bar{A}_{33}$ and added damping $\bar{B}_{33}$ for submergence distance $H/R = 0.809$ with reference data from [19].

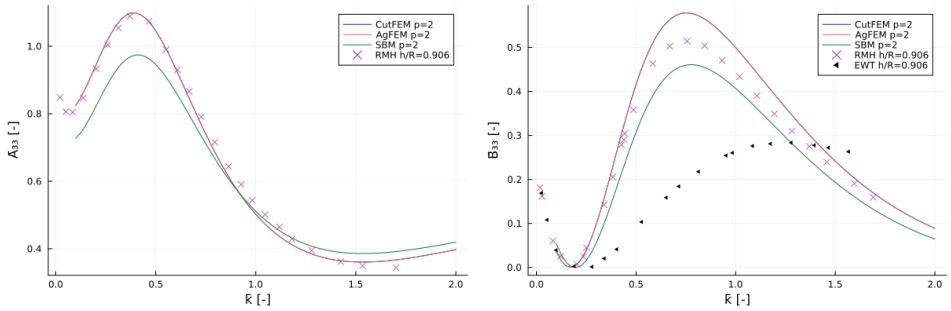

FIGURE 25. Non-dimensional wave number $\bar{k}$ versus non-dimensional added mass $\bar{A}_{33}$ and added damping $\bar{B}_{33}$ for submergence distance $h/R = 0.906$ with reference data from [19].

of order $p = 2$ the results are depicted in Figure 21-25. All unfitted FE methods

appear to follow the trends from the reference data. Especially, for small depths of submergence the results fit to the reference, but for larger submergence depths it appears that the unfitted methods differ more from the added mass and added damping coefficients from the reference. This is likely due to the definition of the reference data which is no longer valid for these submergence depths. The AgFEM and CutFEM results appear to be nearly identical for the cases considered in this study. AgFEM and CutFEM display close to identical results for both first and second order elements. The main differences between these methods will be discussed in the next section. As in the previous case study, the SBM method under- or overestimates the hydrodynamic coefficients, compared to the reference solution. This is more prominent in the added mass coefficient. This can be caused by the lack of resolution of the volume around the object and the loss in accuracy due to the expansion of the gradient. It is especially prevalent for the higher order case, which has fewer elements than the first order setup. Possible measures to mitigate these errors are the use of gradient recovery techniques as proposed in [4] or the weighted SBM proposed in [13, 39]. These two remedies will be further investigated in follow-up works.

4.4. **Matrix conditioning.** In this section, we address the efficiency of each method by discussing the condition number of the block matrix $\mathbb{A}_{w\phi}$. This is the only matrix component that has to be inverted.

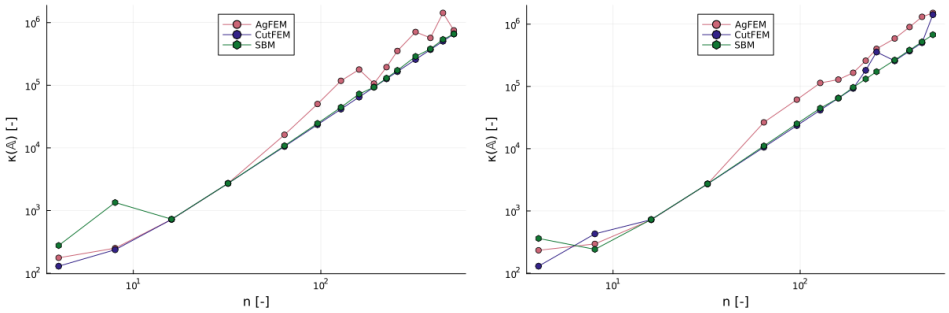

FIGURE 26. Condition number $\kappa(\mathbb{A})$ for varying number of elements n for the rectangle (left) and cylinder (right) case studies.

In Figure 26 the condition number κ is plotted against the number of elements n for the rectangle on the left and the cylinder case study on the right. Generally, AgFEM always appears to have the largest condition number. For CutFEM the condition number is slightly smaller than for SBM, but for a certain number of elements n there is a peak for the cases where there are small cut cells. Especially in Figure 27 this becomes apparent. It depicts the condition number for varying depths of submergence at $n = 128$ where for some cases the CutFEM condition number exceeds the AgFEM condition number. The SBM shows a constant condition number, because of the absence of cut cells by definition.

5. **Conclusions.** In this work we applied CutFEM, AgFEM and SBM as accurate and efficient tools to solve 2D problems using linear potential flow around rigid

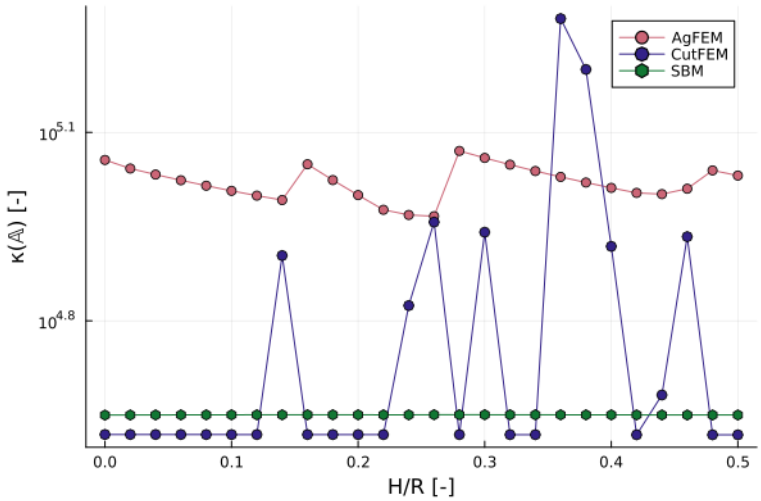

FIGURE 27. Condition number $\kappa(\mathbb{A})$ for varying submergence depth H for the cylinder case study with radius R.

objects for several geometries in the frequency domain. We demonstrate a novel application of CutFEM, AgFEM and SBM using linear potential flow in the frequency domain and how to estimate the added mass and added damping whilst incorporating these methods. For CutFEM a sensitivity study is conducted for the ghost penalty parameter γ and the reference value from literature is deemed sufficient. We highlight efficiency by allowing a single background mesh to simulate several geometrical scenarios with different unfitted FE methods. The condition number is lowest for the CutFEM method, closely followed by SBM, and then AgFEM that has the largest condition numbers. The largest outliers in condition number occur for CutFEM and these are completely absent for SBM. Regarding implementation, AgFEM has the simplest weak form corresponding to the conformal case with a modified FE space. CutFEM requires additional ghost penalty stabilization terms depending on the order p of the elements. Lastly, SBM requires most changes due to the shifting operator and the Jacobian on the embedded object. The ghost penalty stabilization parameter is studied and included in the case studies to reduce the condition number for CutFEM. We highlight the accuracy of the unfitted methods by comparing them with other numerical methods and experimental and analytical reference data. Identifying possible bottlenecks and knowledge gaps for future research. Our results show that the difference in results for the estimation of added mass and added damping is small. For SBM, a gradient recovery technique via mixed formulation should be applied to study the SBM accuracy for linear elements. Additionally, our SBM formulation allows for further research on the correct shifting of the hydrodynamic and hydrostatic pressure terms as these are to be integrated on the true boundary and thus we should shift these Jacobian integral contributions from the true to the surrogate boundary. This contribution should become visible in the matrix term $\mathbb{A}_{v\phi}$ and requires further investigation. A follow-up study investigating the application of a weighted SBM should also be conducted.

REFERENCES

[1] S. Agarwal, O. Colomés, and A. V. Metrikine, Dynamic analysis of viscoelastic floating membranes using monolithic finite element method, *Journal of Fluids and Structures*, **129** (2024), 104167.

[2] G. B. Airy, *Tides and Waves*, B. Fellowes, 1845.

[3] N. M. Atallah, C. Canuto and G. Scovazzi, The second-generation shifted boundary method and its numerical analysis, *Computer Methods in Applied Mechanics and Engineering*, **372** (2020), 113341.

[4] N. M. Atallah, C. Canuto and G. Scovazzi, The shifted boundary method for solid mechanics, *International Journal for Numerical Methods in Engineering*, **122** (2021), 5935-5970.

[5] S. Badia, P. A. Martorell and F. Verdugo, Geometrical discretisations for unfitted finite elements on explicit boundary representations, *Journal of Computational Physics*, **460** (2022), 111162.

[6] S. Badia, E. Neiva and F. Verdugo, Robust high-order unfitted finite elements by interpolation-based discrete extension, *Computers and Mathematics with Applications*, **127** (2022), 105-126.

[7] S. Badia and F. Verdugo, Gridap: An extensible finite element toolbox in julia, *Journal of Open Source Software*, **5** (2020), 2520.

[8] S. Badia, F. Verdugo and A. F. Martín, The aggregated unfitted finite element method for elliptic problems, *Computer Methods in Applied Mechanics and Engineering*, **336** (2018), 533-553.

[9] J. Bezanson, A. Edelman, S. Karpinski and V. B. Shah, Julia: A fresh approach to numerical computing, *SIAM Review*, **59** (2017), 65-98.

[10] H. B. Bingham and H. Zhang, On the accuracy of finite-difference solutions for nonlinear water waves, *Journal of Engineering Mathematics*, **58** (2007), 211-2287.

[11] E. Burman, Ghost penalty, *Comptes Rendus. Mathématique*, **348** (2010), 1217-1220.

[12] E. Burman and P. Hansbo, Fictitious domain finite element methods using cut elements: I. a stabilized lagrange multiplier method, *Computer Methods in Applied Mechanics and Engineering*, **199** (2010), 2680-2686.

[13] O. Colomés, A. Main, L. Nouveau and G. Scovazzi, A weighted shifted boundary method for free surface flow problems, *Journal of Computational Physics*, **424** (2021), 109837.

[14] O. Colomés, F. Verdugo and I. Akkerman, A monolithic finite element formulation for the hydroelastic analysis of very large floating structures, *International Journal for Numerical Methods in Engineering*, **124** (2023), 714-751.

[15] M. Davari, R. Rossi, P. Dadvand, I. Lopez and R. Wüchner, A cut finite element method for the solution of the full-potential equation with an embedded wake, *Computational Mechanics*, **63** (2019), 821-833.

[16] F. de Prenter, C. V. Verhoosel, E. H. van Brummelen, M. G. Larson and S. Badia, Stability and conditioning of immersed finite element methods: Analysis and remedies, *Archives of Computational Methods in Engineering*, **30** (2023), 3617-3656.

[17] A. P. Engsig-Karup, H. B. Bingham and O. Lindberg, An efficient flexible-order model for 3d nonlinear water waves, *Journal of Computational Physics*, **228** (2009), 2100-2118.

[18] C. Geuzaine and J-F. Remacle. Gmsh: A 3-d finite element mesh generator with built-in pre- and post-processing facilities. *International Journal for Numerical Methods in Engineering*, **79** (2009), 1309-13319.

[19] M. Greenhow and S. I. Ahn, Added mass and damping of horizontal circular cylinder sections, *Ocean Engineering*, **15** (1988), 495-504.

[20] P. Hansbo, M. G. Larson and K. Larsson, Cut finite element methods for linear elasticity problems, In *Geometrically Unfitted Finite Element Methods and Applications: Proceedings of the UCL Workshop 2016*, **121** (2017), 25-63.

[21] J. Lee, J. Kim, H. Choi and K-S. Yang, Sources of spurious force oscillations from an immersed boundary method for moving-body problems, *Journal of Computational Physics*, **230** (2011), 2677-2695.

[22] A-J. Li, Y. Liu and H.-J. Li, New analytical solutions to water wave radiation by vertical truncated cylinders through multi-term galerkin method, *Meccanica*, **54** (2019), 429-450.

[23] H. Liang, O. M. Faltinsen and Y. Shao, Application of a 2d harmonic polynomial cell (hpc) method to singular flows and lifting problems, *Applied Ocean Research*, **53** (2015), 75-90.

[24] C-C. Liao, Y-W. Chang, C-A. Lin and J. M. McDonough, Simulating flows with moving rigid boundary using immersed-boundary method, *Computers and Fluids*, **39** (2010), 152-167.
[25] J. Lighthill, Fundamentals concerning wave loading on offshore structures, *Journal of Fluid Mechanics*, **173** (1986), 667–681.
[26] A. Main and G. Scovazzi, The shifted boundary method for embedded domain computations. part i: Poisson and stokes problems, *Journal of Computational Physics*, **372** (2018), 972-995.
[27] P. A. Martorell and S. Badia, High order unfitted finite element discretizations for explicit boundary representations, *Journal of Computational Physics*, **511** (2024), 113127.
[28] J. N. Newman and C. H. Lee, Boundary-element methods in offshore structure analysis, *J. Offshore Mech. Arct. Eng.*, **124** (2002), 81-89.
[29] T. Song, A. Main, G. Scovazzi and M. Ricchiuto, The shifted boundary method for hyperbolic systems: Embedded domain computations of linear waves and shallow water flows, *Journal of Computational Physics*, **369** (2018), 45-79.
[30] C. Tong, Y. Shao, H. B. Bingham and F.-C. W. Hanssen, An adaptive harmonic polynomial cell method with immersed boundaries: Accuracy, stability and applications, *International Journal for Numerical Methods in Engineering*, **122** (2021), 2945-2980.
[31] F. Verdugo and S. Badia, The software design of gridap: A finite element package based on the julia JIT compiler, *Computer Physics Communications*, **276** (2022), 108341.
[32] J. Visbech, A. P. Engsig-Karup, H. B. Bingham, M. Amini-Afshar and M. Ricchiuto, *A High-Order Shifted Boundary Method for Water Waves and Floating Bodies*, In 39th International Workshop on Water Waves and Floating Bodies, 2024.
[33] J. Visbech, A. P. Engsig-Karup and M. Ricchiuto, A spectral element solution of the poisson equation with shifted boundary polynomial corrections: influence of the surrogate to true boundary mapping and an asymptotically preserving robin formulation, *Journal of Scientific Computing*, **102** (2025), 11.
[34] J. H. Vugts, The hydrodynamic coefficients for swaying, heaving and rolling cylinders in a free surface, *International Shipbuilding Progress*, **15** (1968), 251-276.
[35] W. Wang, C. Pákozdi, A. Kamath and H. Bihs, A fully nonlinear potential flow wave modelling procedure for simulations of offshore sea states with various wave breaking scenarios, *Applied Ocean Research*, **117** (2021), 102898.
[36] Y. Wang, Y. Shao, J. Chen and H. Liang, Accurate and efficient hydrodynamic analysis of structures with sharp edges by the extended finite element method (xfem): 2d studies, *Applied Ocean Research*, **117** (2021), 102893.
[37] G. X. Wu and R. E. Taylor, Finite element analysis of two-dimensional non-linear transient water waves, *Applied Ocean Research*, **16** (1994), 363-372.
[38] G. X. Wu and R. E. Taylor, Time stepping solutions of the two-dimensional nonlinear wave radiation problem, *Ocean Engineering*, **22** (1995), 785-798.
[39] D. Xu, O. Colomés, A. Main, K. Li, N. M. Atallah, N. Abboud and G. Scovazzi, A weighted shifted boundary method for immersed moving boundary simulations of stokes' flow, *Journal of Computational Physics*, **510** (2024), 113095.
[40] Y. Xu, H. B. Bingham and Y. Shao, Finite difference solutions for nonlinear water waves using an immersed boundary method, *International Journal for Numerical Methods in Fluids*, **93** (2021), 1143-1162.
[41] Y. Xu, H. B. Bingham and Y. Shao, A high-order finite difference method with immersed-boundary treatment for fully-nonlinear wave-structure interaction, *Applied Ocean Research*, **134** (2023), 103535.

Received December 2024; revised April 2025.